

## Strain Effects in a Directly Bonded Diamond-on-Insulator Substrate

Varveris, Ioannis; Aliberti, Gianni D.; Chen, Tianyin; Sfetcu, Filip A.; Dekker, Diederik J.W.; Schuurmans, Alfred; Nitzsche, Nikolaj K.; Nur, Salahuddin; Ishihara, Ryoichi

**DOI**

[10.1002/pssa.202500277](https://doi.org/10.1002/pssa.202500277)

**Publication date**

2025

**Document Version**

Final published version

**Published in**

Physica Status Solidi (A) Applications and Materials Science

**Citation (APA)**

Varveris, I., Aliberti, G. D., Chen, T., Sfetcu, F. A., Dekker, D. J. W., Schuurmans, A., Nitzsche, N. K., Nur, S., & Ishihara, R. (2025). Strain Effects in a Directly Bonded Diamond-on-Insulator Substrate. *Physica Status Solidi (A) Applications and Materials Science*. <https://doi.org/10.1002/pssa.202500277>

**Important note**

To cite this publication, please use the final published version (if applicable).  
Please check the document version above.

**Copyright**

Other than for strictly personal use, it is not permitted to download, forward or distribute the text or part of it, without the consent of the author(s) and/or copyright holder(s), unless the work is under an open content license such as Creative Commons.

**Takedown policy**

Please contact us and provide details if you believe this document breaches copyrights.  
We will remove access to the work immediately and investigate your claim.

# Strain Effects in a Directly Bonded Diamond-on-Insulator Substrate

Ioannis Varveris,\* Gianni D. Aliberti, Tianyin Chen, Filip A. Sfetcu, Diederik J. W. Dekker, Alfred Schuurmans, Nikolaj K. Nitzsche, Salahuddin Nur, and Ryoichi Ishihara

The direct bonding process of a diamond-on-insulator (DOI) substrate enables monolithic integration of diamond photonic structures for quantum computing by improving photon collection efficiency and entanglement generation rate between emitters. It also addresses key fabrication challenges, such as robustness, bonding strength, and scalability. This study investigates strain effects in DOI substrates following direct bonding. Strain generation is expected near the diamond–SiO<sub>2</sub>/Si interface due to the thermal expansion coefficient mismatch between the bonded materials. Strain-induced lattice distortions are characterized using nitrogen-vacancy (NV) centers in diamond via optically detected magnetic resonance (ODMR) and photoluminescence (PL) mapping. PL mapping reveals interference fringes in unbonded regions, indicating bonding irregularities. Depth-resolved ODMR measurements show a volumetric strain component increase of  $\approx 0.45$  MHz and a shear component increase of  $\approx 0.71$  MHz between the top surface and the DOI interface. However, ODMR signal contrast and peak linewidth remain largely unaffected, suggesting no visible deterioration in the optical properties of the emitters. By combining ODMR and PL mapping, this work establishes a robust methodology for assessing bonding quality and strain impact on NV centers, an essential step toward advancing scalable quantum technologies and integrated photonic circuits.

## 1. Introduction

One of the challenges in achieving robust quantum communication and high-fidelity quantum computing has long been the entanglement generation rate between nitrogen-vacancy (NV) centers, which is limited by the relatively low fraction of emitted coherent photons that can be detected. A solution to address this problem is to integrate NV centers into optical cavities with a high ratio of quality factor to mode volume. This is done to increase the zero-phonon line emission and improve collection efficiency.<sup>[1]</sup>

However, current applications are limited by the challenges of growing large single-crystal diamond (SCD) via chemical vapor deposition (CVD), which restricts its use in integrated photonics.<sup>[2]</sup> To overcome this, researchers are developing thin film diamond integrated with color centers in photonic crystal cavities.<sup>[3]</sup> Two prominent approaches are hybrid and monolithic all-diamond systems.<sup>[4]</sup> Hybrid systems use nondiamond materials like silicon nitride or gallium phosphide coupled with diamond color centers for easier manufacturing and integration.<sup>[5–7]</sup>


Nevertheless, they face issues with limited coupling efficiency. Monolithic all-diamond systems, which entail fabricating optical cavities directly on SCD substrates, have shown success with not only NV,<sup>[8]</sup> but also SiV,<sup>[9,10]</sup> and GeV centers.<sup>[8]</sup>

Such a monolithic fabrication technique is the direct bonding of diamond-on-insulator substrates. Hydrophilic (water-attracting) direct bonding, in particular, is preferred over indirect methods using adhesives, due to its high bonding strength, temperature stability, and industrial scalability.<sup>[11]</sup> Similar to silicon-on-insulator (SOI) substrate bonding,<sup>[12]</sup> Diamond-on-insulator (DOI) bonding adheres to the same operating principles. After the surface of the diamond and the insulator (in this case SiO<sub>2</sub>) have been activated, they are then brought into contact, in order for them to create a bond, as a result of van der Waals forces, and form covalent bonds.<sup>[12]</sup> The material is subsequently annealed in order to enhance the quality of the interface.<sup>[13]</sup>

However, despite the effectiveness of direct bonding and subsequent annealing in enhancing interface quality, this fabrication process can introduce unintended strain effects within the

I. Varveris, G. D. Aliberti, F. A. Sfetcu, A. Schuurmans, N. K. Nitzsche, R. Ishihara  
 QuTech  
 Delft University of Technology  
 Lorentzweg 1, 2628 CJ Delft, The Netherlands  
 E-mail: i.varveris@tudelft.nl

I. Varveris, G. D. Aliberti, T. Chen, D. J. W. Dekker, N. K. Nitzsche, S. Nur, R. Ishihara  
 Department of Quantum and Computer Engineering  
 Delft University of Technology  
 Mekelweg 4, 2628 CD Delft, The Netherlands

 The ORCID identification number(s) for the author(s) of this article can be found under <https://doi.org/10.1002/pssa.202500277>.

© 2025 The Author(s). physica status solidi (a) applications and materials science published by Wiley-VCH GmbH. This is an open access article under the terms of the Creative Commons Attribution License, which permits use, distribution and reproduction in any medium, provided the original work is properly cited.

DOI: 10.1002/pssa.202500277

diamond structure. It is probable that the diamond, having undergone the aforementioned chemical processing, will exhibit further stress effects on the surface that is bonded to the insulator substrate. Furthermore, part of the direct bonding process takes place at a temperature of 200 °C. During the cooling period, each of the bonded materials contracts at different rates, according to their unique thermal expansion coefficients. This mismatch between the thermal expansion rates of the diamond and the silicon dioxide/silicon can lead to the generation of strain at their interface,<sup>[14,15]</sup> and potentially further deep into the diamond lattice.

These strain effects can cause deformations to the crystal lattice, which result in inhomogeneous broadening and degradation of the spin dephasing time of the NV centers. Therefore, it is deemed critical to be able to understand and visually map the effects of strain, providing meaningful insight into the quality of the bonded samples.

## 2. Direct Bonding Process Overview

The fabrication of the DOI substrate utilized in this work follows a hydrophilic direct bonding process, outlined in **Figure 1**. No adhesives were used in the bonding, which relied entirely on surface chemical activation and low-temperature annealing to achieve interfacial adhesion.

Hydrophilic direct bonding is a process that involves creating a bond between surfaces treated to exhibit hydrophilic properties. The first step is surface activation, which prepares the surfaces for subsequent bonding by introducing reactive hydroxyl groups (–OH). For the diamond substrate, this involves thorough cleaning using a Piranha solution, a highly

oxidative mixture of sulfuric acid (H<sub>2</sub>SO<sub>4</sub>) and hydrogen peroxide (H<sub>2</sub>O<sub>2</sub>) in a 3:1 ratio. The Piranha solution does not etch the diamond, but removes organic contamination and promotes surface hydrophilicity. This process results in the termination of the diamond surface with hydroxyl groups (C–OH), enhancing its reactivity by providing essential reactive sites for bonding with other molecules and facilitating further chemical reactions.<sup>[13,16]</sup>

The insulator substrate is composed of a 300 nm, plasma-enhanced chemical vapor deposition (PECVD)-grown layer of SiO<sub>2</sub> on Si. Hydrophilic bonding relies on the formation of silanol (Si–OH) groups on the SiO<sub>2</sub> surface. Therefore, following rinsing of the SiO<sub>2</sub>/Si substrate with deionized (DI) water, it undergoes O<sub>2</sub> plasma treatment, a common method for cleaning and oxidizing silicon surfaces.<sup>[13]</sup> This treatment both removes surface contamination and increases silanol group density by oxidizing siloxane (Si–O–Si) bridges in the presence of water vapor. These hydroxyl-terminated surfaces are hydrophilic and attract adsorbed water molecules from the environment.

Once activated, both the diamond and SiO<sub>2</sub>/Si surfaces become highly hydrophilic due to the formation of surface hydroxyl (–OH) groups. This promotes the adsorption of ambient water molecules, leading to the formation of a thin hydration layer on each surface. When the substrates are brought into contact under ambient conditions, hydrogen bonding and van der Waals interactions across this interfacial water layer enable initial adhesion and stabilize the alignment of the surfaces (see **Figure 2**). Specifically, hydroxyl groups such as C–OH and Si–OH participate in hydrogen bonding, which, although individually weak, collectively contribute significantly to the mechanical integrity of the interface.<sup>[17]</sup>

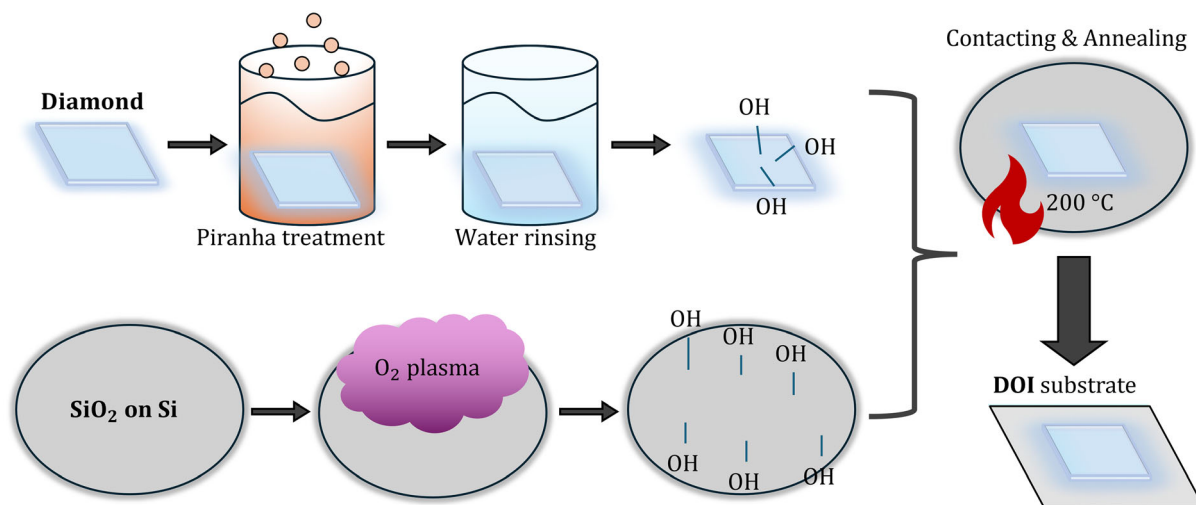


**Figure 1.** Schematic overview of the hydrophilic direct bonding process used to fabricate the DOI substrate. The process begins with a type Ib, single-crystal, double-side polished, (100)-oriented diamond substrate, and a Si substrate, coated with a 300 nm SiO<sub>2</sub> layer, and diced into 25 × 25 mm<sup>2</sup> chips. Both substrates undergo chemical activation. The diamond is cleaned using Piranha solution (3:1 H<sub>2</sub>SO<sub>4</sub>:H<sub>2</sub>O<sub>2</sub>) at 75 °C for 30 min and rinsed in DI water for 5–10 min. Meanwhile, the SiO<sub>2</sub>/Si substrate is rinsed with DI water for 5 min, and is then subjected to O<sub>2</sub> plasma treatment (1000 W, 5 min, with 400 sccm O<sub>2</sub> flow) using a PVA Tepla system. These steps remove surface contaminants and enrich the surface with silanol (Si–OH) groups, promoting hydrophilicity. After cleaning, the substrates are brought into contact at room temperature (20 °C) and ambient humidity (≈40%), allowing van der Waals and hydrogen bonding to form across a thin interfacial water layer. This prebonding interaction is stabilized through a low-temperature anneal at 200 °C for 24 h, under N<sub>2</sub> flow. The annealing induces interfacial dehydration, resulting in covalent bond formation, thus completing the DOI heterostructure. The bonded stack typically exhibits high mechanical integrity with no visible voids or delamination.

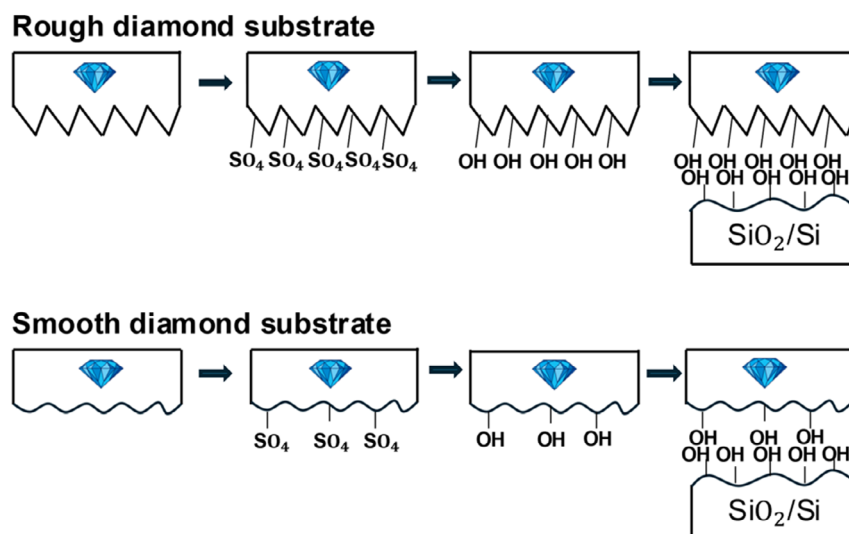
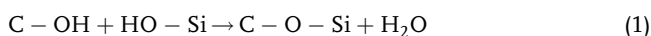


**Figure 2.** Illustration of the interfacial bonding mechanism between diamond and  $\text{SiO}_2$ . Increased surface roughness enhances the density of hydroxyl ( $-\text{OH}$ ) terminations, facilitating more effective hydrogen bonding and improving the overall bonding success. Reproduced with permission from Chen et al.<sup>[11]</sup> 2025, AIP Publishing.

Following initial contact, the DOI stack undergoes annealing, with temperature and duration serving as critical parameters for achieving robust interfacial bonding. Utilizing low-temperature annealing at  $200^\circ\text{C}$ , the bond strength is enhanced through dehydration reactions between adjacent silanol groups, producing strong  $\text{Si}-\text{O}-\text{C}$  covalent bridges across the interface.<sup>[17]</sup> This irreversible covalent bonding process completes the formation of the DOI heterostructure, as expressed by the reaction seen below.



Throughout this process, care was taken to maintain surface roughness within an optimal range. The surface roughness values of the diamond and the  $\text{SiO}_2/\text{Si}$  substrate fall within the 2–5 nm range typically reported as suitable for reliable hydrophilic bonding.<sup>[11]</sup> Notably, no high-temperature processing or aggressive etching was applied that could significantly modify surface topography prior to bonding.

The bonded interface remains intact through post-processing steps, and no delamination or void formation is typically observed. This is consistent with the formation of strong interfacial bonds and the maintenance of a mechanically coherent interface. The process flow has been replicated multiple times, further validating its general applicability and reproducibility.

### 3. Strain Effects in the Diamond-on-Insulator System

#### 3.1. Origin and Mechanisms of Strain in Directly Bonded DOI Structures

The direct bonding process of a DOI substrate inevitably induces strain at the interface, with the most significant contribution arising from thermal expansion mismatch between the bonded materials<sup>[15]</sup> since prior to bonding, the residual stress in both

the diamond and  $\text{SiO}_2/\text{Si}$  substrates is minimal.<sup>[18]</sup> The diamond used did not undergo post-growth annealing or epitaxy, which would otherwise introduce nonuniform stress.<sup>[19]</sup> Additionally, optical inspection revealed no bowing, indicating negligible macroscopic stress. Similarly, the underlying substrate remains mechanically relaxed.<sup>[18]</sup> Any pre-existing uniform residual stress is accounted for as a constant offset in the optically detected magnetic resonance (ODMR) measurements, as the observed strain is induced post-bonding.

The annealing process at  $200^\circ\text{C}$ , necessary for bond stabilization, introduces thermal strain in the DOI heterostructure upon cooling to room temperature. This strain arises due to the mismatch in thermal expansion coefficients between the constituent materials. Diamond exhibits a low thermal expansion coefficient, with  $\alpha_{\text{D}} \approx 1.1 \times 10^{-6} \text{ K}^{-1}$  at room temperature and  $\alpha_{\text{D}} \approx 2.3 \times 10^{-6} \text{ K}^{-1}$  at  $200^\circ\text{C}$ .<sup>[20]</sup> In contrast, amorphous silica ( $\text{SiO}_2$ ) has an expansion coefficient of  $\alpha_{\text{SiO}_2} \approx 2.5 \times 10^{-6} \text{ K}^{-1}$  at room temperature<sup>[21]</sup> and  $\alpha_{\text{SiO}_2} \approx 3.0 \times 10^{-6} \text{ K}^{-1}$  at  $200^\circ\text{C}$ .<sup>[21,22]</sup> Silicon, on the other hand, expands significantly more than diamond, with  $\alpha_{\text{Si}} \approx 2.6 \times 10^{-6} \text{ K}^{-1}$  at room temperature and  $\alpha_{\text{Si}} \approx 3.3 \times 10^{-6} \text{ K}^{-1}$  at  $200^\circ\text{C}$ .<sup>[23,24]</sup> Table 1 summarizes the relevant thermal expansion coefficients. Since the  $\text{SiO}_2$  layer is only 300 nm thick, while the underlying Si substrate is several hundred microns thick, the thermal and mechanical behavior of the bonded insulator stack is dominated by the silicon. The

**Table 1.** Linear thermal expansion coefficients ( $\alpha$ ) of materials in the DOI stack.

Material	$\alpha$ (RT) ( $\times 10^{-6} \text{ K}^{-1}$ )	$\alpha$ ( $200^\circ\text{C}$ ) ( $\times 10^{-6} \text{ K}^{-1}$ )
Diamond	$\approx 1.1$	$\approx 2.3$
PECVD $\text{SiO}_2$	$\approx 2.5$	$\approx 3.0$
Silicon	$\approx 2.6$	$\approx 3.3$

diamond layer, in turn, is constrained by this underlying Si substrate across the interfacial SiO<sub>2</sub> layer, which behaves elastically under these conditions. Upon cooling, the Si substrate contracts more than the diamond, imposing compressive in-plane strain on the diamond layer.<sup>[25]</sup> For a temperature drop of  $\Delta T \approx 180$  K, the resulting in-plane thermal mismatch strain is estimated as  $\varepsilon \approx (\alpha_{\text{Si}}^{200^\circ\text{C}} - \alpha_{\text{D}}^{200^\circ\text{C}})\Delta T \approx -1.8 \times 10^{-4}$ .

While the SiO<sub>2</sub> layer serves as the direct interface between diamond and Si, it is important to consider whether it could act as a strain-relieving buffer. In particular, viscous relaxation or interfacial slippage could potentially mitigate strain transfer. However, previous studies report that viscous flow in SiO<sub>2</sub> requires temperatures above 900–950 °C,<sup>[26]</sup> well beyond the 200 °C annealing conditions used here. At these lower temperatures, the oxide behaves elastically. Moreover, the formation of covalent interfacial bonds effectively suppresses slippage at the diamond–SiO<sub>2</sub> interface.<sup>[11]</sup> As a result, the bonded stack behaves as a mechanically coherent system, with strain transmitted directly from the silicon substrate to the diamond through the thin, elastically deforming oxide layer.

Surface roughness is another potential contributor to strain. However, in our study, the bonded diamond surface had an initial roughness of  $R_a < 2$  nm, preserved through the Piranha and DI water cleaning steps. O<sub>2</sub> plasma etching was applied to the unbonded top diamond surface, with no measurable change in surface roughness. The SiO<sub>2</sub> layer had a measured root mean square (RMS) roughness of  $S_q = 4.44$  nm prior to bonding. Both these values fall within the 2–5 nm range considered suitable for uniform bonding.<sup>[11]</sup>

Finally, localized surface defects, such as scratches or implantation damage, are known to produce sharp strain gradients and localized ODMR shifts.<sup>[27]</sup> In contrast, the strain fields observed in our bonded samples are spatially extended and homogeneous over tens of microns, without any localized stress anomalies. Delamination is also not typically observed following this direct bonding process. These features are inconsistent with surface-defect-induced strain, and instead match the expected thermo-mechanical strain distribution in a bonded multilayer stack. Therefore, the strain analyzed in this work originates predominantly from thermal expansion mismatch, transmitted through the SiO<sub>2</sub> layer without significant relaxation.

### 3.2. Strain Physics in NV Centers

The Hamiltonian  $\hat{H}$  of the ground-state spin triplet state of the NV center in diamond, in the absence of imperfections (no strain) and external fields, can be described by the electron spin–spin interaction, which arises from second-order perturbation theory applied to the spin–orbit interaction.<sup>[28]</sup> Defining the z-axis along the NV-axis results in the following expression for the Hamiltonian:

$$\frac{\hat{H}}{h} = DS_z^2 \quad (2)$$

where  $h$  is Planck's constant,  $\mathbf{S}$  is the spin operator of the NV center, and  $D = 2.87$  GHz is the zero-field splitting (ZFS) tensor.

#### 3.2.1. Spin–Strain Interaction

In reality, numerous imperfections exist within the diamond lattice, making the spin–strain interaction non-negligible. According to Udvarhelyi et al.<sup>[29]</sup> the spin–strain interaction for the ground-state spin triplet can be described as a deformation in the diamond crystal, causing the strain tensor  $\varepsilon_{ij}$  to couple to the NV spin through the symmetry-allowed Hamiltonian.

$$\hat{H}_\varepsilon = \hat{H}_\varepsilon^0 + \hat{H}_\varepsilon^1 + \hat{H}_\varepsilon^2 \quad (3)$$

where each term couples to different spin transitions.  $\hat{H}_\varepsilon^0$  concerns the  $|m_S = 0\rangle$  to  $|m_S = 0\rangle$  transition (shifting or splitting the  $|m_S = 0\rangle$  level),  $\hat{H}_\varepsilon^1$  the  $|m_S = 0\rangle$  to the  $|m_S = \pm 1\rangle$  transition, and  $\hat{H}_\varepsilon^2$  the  $|m_S = \pm 1\rangle$  to the  $|m_S = -1\rangle$  transition.

In the NV reference frame ( $x, y, z$ ), aligned so that  $z$  is the NV-axis and ( $x, y$ ) spans the perpendicular plane, the general spin–strain Hamiltonian allowed by the  $C_{3v}$  symmetry is written as<sup>[29]</sup>

$$\begin{aligned} \hat{H}_\varepsilon/h = & \left\{ [h_{41}(\varepsilon_{xx} + \varepsilon_{yy}) + h_{43}\varepsilon_{zz}] S_z^2 \right. \\ & + \frac{1}{2} \left[ h_{26}\varepsilon_{zx} - \frac{1}{2}h_{25}(\varepsilon_{xx} - \varepsilon_{yy}) \right] \{S_x, S_z\} \\ & + \frac{1}{2} [h_{26}\varepsilon_{yz} + h_{25}\varepsilon_{xy}] \{S_y, S_z\} \\ & + \frac{1}{2} \left[ h_{16}\varepsilon_{zx} - \frac{1}{2}h_{15}(\varepsilon_{xx} - \varepsilon_{yy}) \right] (S_y^2 - S_x^2) \\ & + \frac{1}{2} [h_{16}\varepsilon_{yz} + h_{15}\varepsilon_{xy}] \{S_x, S_y\} \\ & \equiv M_z S_z^2 + N_x \{S_x, S_z\} + N_y \{S_y, S_z\} \\ & \left. + M_x (S_y^2 - S_x^2) + M_y \{S_x, S_y\} \right\} \end{aligned} \quad (4)$$

where  $h_{ij}$  are coupling parameters (in units of GHz strain<sup>−1</sup>) that depend on the microscopic electronic structure of the NV center (see Table 2),  $M_x$ ,  $M_y$ , and  $M_z$  are the strain tensor amplitudes (in MHz) and  $N_x$ ,  $N_y$  are nondiagonal strain terms that induce coupling between  $|m_S = 0\rangle$  and the  $|m_S = \pm 1\rangle$  states, and  $\varepsilon_{ij}$  is the strain tensor, with  $\mathbf{u}(\mathbf{r})$  being the displacement field.

$$\varepsilon_{ij} = \frac{1}{2} \left( \frac{\partial u_i}{\partial x_j} + \frac{\partial u_j}{\partial x_i} \right) \quad (5)$$

**Table 2.** Spin–strain ( $h$ ) coupling-strength parameters calculated from density functional theory by Udvarhelyi et al.<sup>[29]</sup>

Parameter	Value (MHz strain <sup>−1</sup> )
$h_{43}$	2300 ± 200
$h_{41}$	−6420 ± 90
$h_{25}$	−2600 ± 80
$h_{26}$	−2830 ± 70
$h_{15}$	5700 ± 200
$h_{16}$	19 660 ± 90

If the resulting strain-induced mixing between  $m_s = 0$  and  $m_s = \pm 1$  states is small compared to the zero-field splitting  $D$ , the off-diagonal components  $N_x$ ,  $N_y$  may then be treated as a small perturbation and be neglected.

### 3.2.2. Eigenfrequencies Including the Zeeman Term

In the presence of a homogeneous magnetic field  $\mathbf{B}$ , the NV Hamiltonian acquires an extra term

$$\frac{\hat{H}_B}{h} = \gamma \mathbf{B} \cdot \mathbf{S} \quad (6)$$

where  $\gamma$  is the electron gyromagnetic ratio,  $2.8 \text{ MHz G}^{-1}$ . After diagonalizing this matrix and including the spin-strain interaction Hamiltonian, the following equation is obtained

$$f_{\pm} = D + M_z \pm \sqrt{(\gamma B_z)^2 + M_x^2 + M_y^2} \quad (7)$$

where  $f_{\pm}$  is the frequency of each spin transition. From Equation (6), the following relations can be derived

$$\Delta f_{\text{shift}} = \frac{1}{2}(f_+ + f_-) - D = M_z \quad (8)$$

where  $M_z$  is the volumetric (axial) strain amplitude, quantifying lattice compression or expansion along the NV center axis, directly affecting the resonance frequency shift observed in ODMR measurements, and

$$\Delta f_{\text{split}} = f_+ - f_- = 2\sqrt{(\gamma B_z)^2 + M_x^2 + M_y^2} \quad (9)$$

where  $M_x$  and  $M_y$  represent the shear (transverse) strain components, corresponding to lattice distortions perpendicular to the NV-axis. These transverse components primarily influence the magnitude of peak splitting in the ODMR spectra. Therefore, the effects of strain can be directly characterized by ODMR<sup>[30]</sup> as lattice distortions lead to measurable frequency shifts and splittings of the spin resonance transitions.

## 4. Experimental Section

The primary objective of this study is to measure the effects of strain in diamonds that have undergone direct bonding with an insulator ( $\text{SiO}_2/\text{Si}$ ) substrate. To achieve this, NV centers are used due to their excellent properties that make them highly sensitive to external magnetic fields and strain fields. As already described above, strain can cause splitting and shifts in the energy levels of NV centers. To enable these measurements, a confocal ODMR setup is used, as seen in **Figure 3**. With ODMR, these changes in the energy states and spins can be quantified in the form of the presence of magnetic, electric, strain, or temperature variations. The frequency shift  $\Delta f_{\text{shift}}$  and frequency splitting  $\Delta f_{\text{split}}$  are related to the strain tensor components  $\varepsilon_{ij}$ , through Equation (3).

Solving Equation (7) for  $M_z$  gives

$$M_z = \Delta f_{\text{shift}} \quad (10)$$

while solving Equation (8) for the results in

$$M_{xy} = \sqrt{\frac{\Delta f_{\text{split}}^2}{4} - (\gamma B_z)^2} \quad (11)$$

Therefore, by measuring the strain amplitudes ( $M_x$ ,  $M_y$ ,  $M_z$ ) through ODMR measurements, one can partially reconstruct the strain tensor. Specifically, the volumetric strain component,  $M_z$ , provides a linear combination of the axial strain terms ( $\varepsilon_{xx}$ ,  $\varepsilon_{yy}$ , and  $\varepsilon_{zz}$ ), weighted according to their orientation with respect to the NV center's crystallographic axis. In this research, the difference in values for  $M_{xy}$  and  $M_z$  is acquired after comparing ODMR-obtained spectra at different depths of the diamond's volume, as illustrated in **Figure 4**.

For the experiment, a  $10 \times 10 \text{ mm}^2$  bulk diamond substrate (supplied by EDP), with a thickness of  $\approx 300 \mu\text{m}$ , is investigated, hereafter referred to as  $\text{DS}_{\text{PB}}$ . It is a CVD-grown substrate, cut along the  $\{100\}$  crystallographic plane, that contains randomly distributed ensembles of NV centers with a concentration of roughly 15 ppb. The diamond substrate was double-sided polished, exhibiting an initial surface roughness of  $R_a < 2 \text{ nm}$ , as specified by the supplier. The  $\text{SiO}_2$  surface on the Si wafer, prior to bonding, exhibited a RMS roughness of  $S_q = 4.44 \text{ nm}$ , as measured by AFM.

The top (unbonded) surface of the diamond was later etched by  $\approx 50 \mu\text{m}$ , using  $\text{O}_2$  plasma, with no considerable change to surface roughness, in order to allow focusing on the back surface (diamond- $\text{SiO}_2/\text{Si}$  interface). This challenge arose due to the objective lens' small working distance of  $400 \mu\text{m}$  and the  $100 \mu\text{m}$  diameter of the microwave delivery wire, which is placed between the objective and the piezo stage. Although the refractive index of diamond,  $n = 2.4$ , provides some leniency by modifying the effective distance of the objective-to-diamond, further etching of the surface ensures that proper focus on the back surface can be achieved and eliminates any worries of collision of the diamond with the objective during 2D scanning.

This diamond sample underwent the direct bonding process, but, due to its large surface area, the result was partial bonding of the DOI substrate, meaning that two regions of interest are present—both bonded and unbonded—on the same sample. Different strain fields may exist in these regions, since only part of their surface formed a strong bond with the insulator substrate underneath it. This bonded region has potentially experienced increased strain effects compared to the unbonded one. By comparing the ODMR peak splitting and frequency shift values at the top surface and at the bottom surface (diamond- $\text{SiO}_2/\text{Si}$  interface), an overall increase in strain is observed in the interface.

It should be noted that the following measurements are performed in the presence of an external bias magnetic field  $B_z = 15.7 \text{ G}$  (or  $43.9 \text{ MHz}$  splitting) along the  $z$ -axis. A  $532 \text{ nm}$  green laser is used for optical excitation, at a power of  $0.25 \text{ mW}$ , and the emitted fluorescence is collected via a single-photon counting module (SPCM) (COUNT-10C-FC), coupled to a fiber.

## 5. Results and Discussion

In **Figure 5**, differences in the acquired photoluminescence (PL) maps of the top and back surfaces are visible. During the direct bonding process, even with thorough cleaning of the substrates

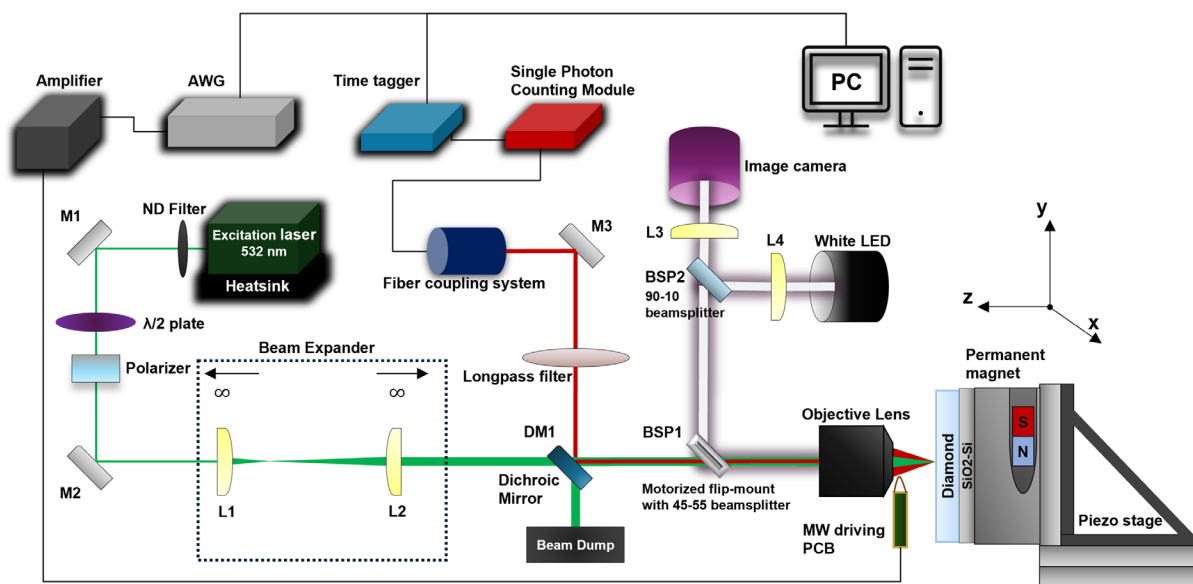


**Figure 3.** Schematic illustration of the confocal ODMR setup used in this work. A 532 nm CW-laser provides optical excitation of the NV centers, with fluorescence collected via a high-NA objective and directed through a dichroic mirror and filters to a SPCM. Microwave excitation is delivered via a wire loop placed near the diamond surface. A bias magnetic field ( $B_z$ ) is applied along the NV-axis to lift spin degeneracy, enabling detection of frequency shifts and splittings associated with strain.

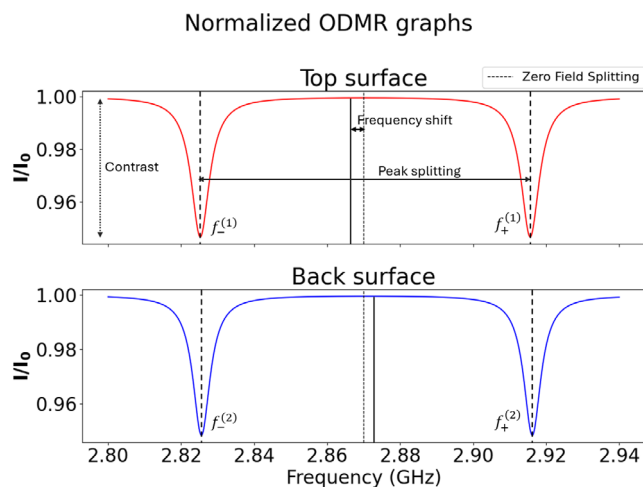


**Figure 4.** Indicative ODMR spectra obtained at the top and at the back surface.

in a cleanroom environment, trapped particles or residues at the diamond-SiO<sub>2</sub>/Si interface may still remain, hindering proper bonding and inducing localized strain regions. This effect is particularly pronounced in the sample investigated here, owing to its large size of  $10 \times 10 \text{ mm}^2$ .

The bonded and unbonded regions can be clearly distinguished, providing a useful tool for evaluating the success and quality of the direct bonding process. Specifically, interference fringes are more apparent in the PL map closer to the bottom surface. This may indicate the presence of particles or impurities that were either not thoroughly rinsed or introduced during one of the direct bonding steps, and subsequently became trapped at

the interface. Such particles could hinder proper adhesion and potentially lead to localized unbonded regions. These regions are linked to nonuniform bonding or strain effects that can alter the observed layer thickness and local refractive index. The direct bonding quality has to be improved, especially regarding substrates with larger surfaces. This would enable high-quality, reproducible bonding and more precise strain mapping.

Afterward, 2D ODMR maps were obtained, starting with a  $60 \times 60 \mu\text{m}^2$  area at the top surface, and then focusing on the diamond plane close to the diamond-SiO<sub>2</sub>/Si interface. **Figure 6** represents volumetric strain variation, obtained by calculating the frequency shift  $\Delta f_{\text{shift}}$  of every point in the map, relative to the ZFS value of  $D = 2.87 \text{ GHz}$ , and solving for  $M_z$ , as seen in Equation (9).

The milder volumetric strain effects at the top surface are attributed to intrinsic strain in the diamond. However, moving closer toward the back surface shows increased strain effects, which are assumed to have been caused by the thermal expansion mismatch that occurs during the direct bonding process.

Similarly, **Figure 7** demonstrates the spatial variation of shear (transverse) strain, obtained via 2D ODMR mapping by analyzing the peak splitting at each measurement point according to Equation (10). Calculating the transverse strain amplitude ( $M_{xy}$ ) reveals the magnitude of lattice distortions in planes perpendicular to the NV-axis (i.e., the  $xy$ ,  $yz$ , and  $xz$  planes). An increase in shear strain is observed near the diamond-SiO<sub>2</sub>/Si interface, consistent with expectations based on the thermal expansion coefficient mismatch between the bonded materials.

Next, ODMR measurements were performed at various depths ( $z$ -axis scans), starting from the top surface of the DS<sub>PB</sub> sample and finishing close to the bottom surface (diamond-SiO<sub>2</sub>/Si interface). These ODMR measurements provide

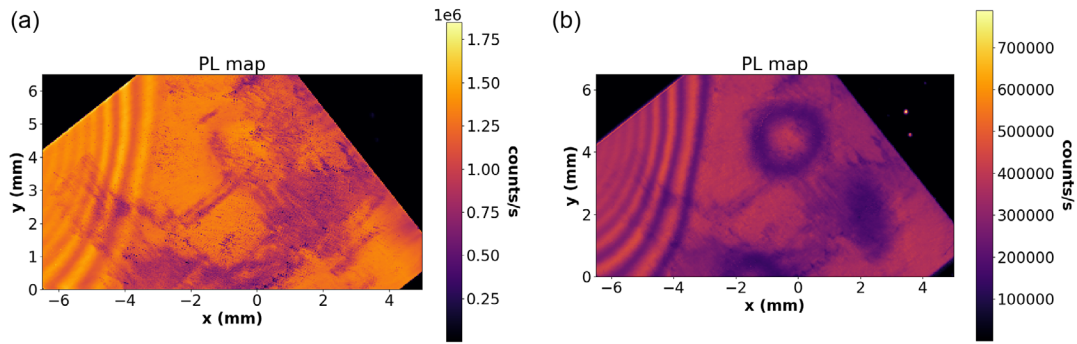


**Figure 5.** Coarse PL maps of the partially bonded diamond substrate. a) Top surface, b) Back surface.

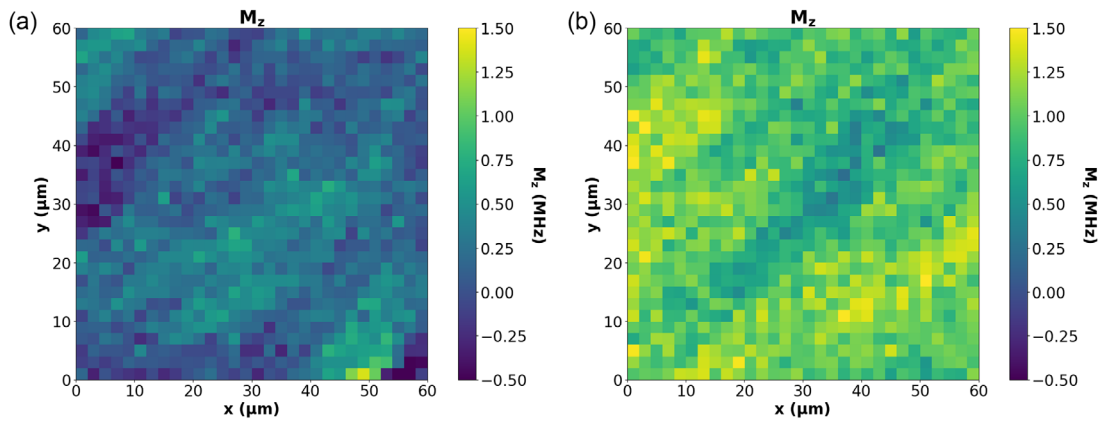


**Figure 6.** ODMR 2D scans performed in a  $60 \times 60 \mu\text{m}^2$  area, depicting the effects of the volumetric strain amplitude  $M_z$ . a) Top surface, b) Back surface.

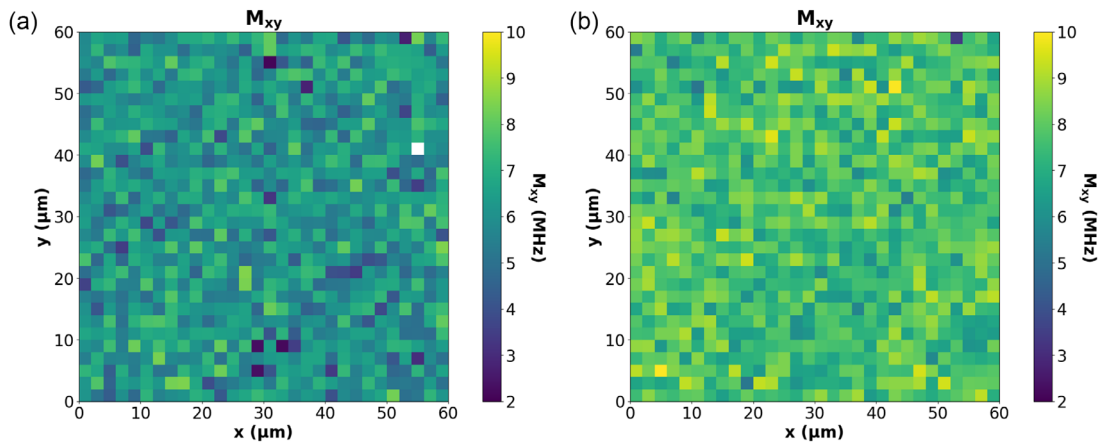


**Figure 7.** ODMR 2D scans performed in a  $60 \times 60 \mu\text{m}^2$  area, depicting the effects of the transverse strain amplitude  $M_{xy}$ . a) Top surface, b) Back surface.

information on multiple quantities, such as the frequency shift, which is related to volumetric strain, the frequency splitting, related to shear strain, and ODMR peak contrast, which provides insight into the signal-to-noise ratio (SNR) and peak broadening. These measurements include data from both bonded and seemingly unbonded regions.

In **Figure 8**, a gradual increase in both volumetric and shear strain can be seen. Contrary to the 2D ODMR maps discussed earlier, such a measurement allows a direct observation of how the strain effects are increasingly more intense close to the interface. Values of  $M_z$  range from 0.11 MHz up to 0.56 MHz, whereas values of  $M_{xy}$  range from 10.05 to 10.76 MHz.

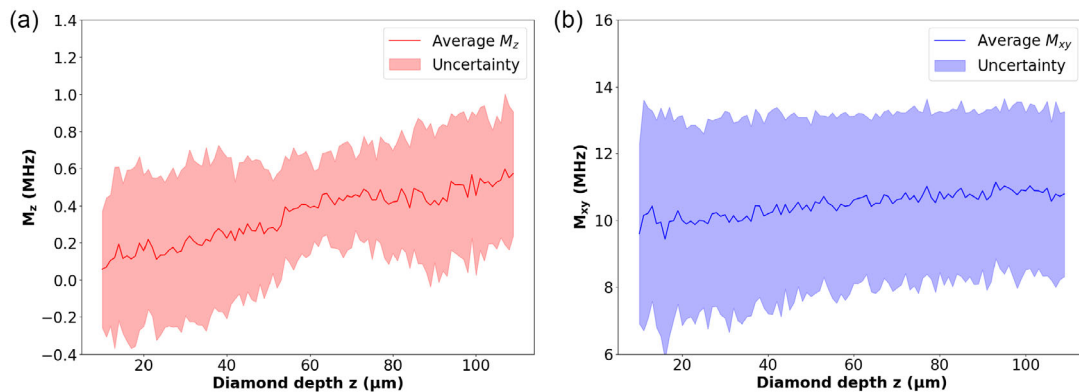


**Figure 8.** Data from different ODMR graphs, obtained at varying planes of the diamond substrate. The data is averaged out of nine different ODMR scans, each starting from a different region of the surface of the diamond. a) Shows the increase of the  $M_z$  parameter, acquired via frequency shift compared to the default ZFS value in ODMR measurements, and corresponding to volumetric strain, and b) shows the increase of the  $M_{xy}$  parameter, acquired via peak splitting in ODMR measurements, and corresponding to shear strain components.

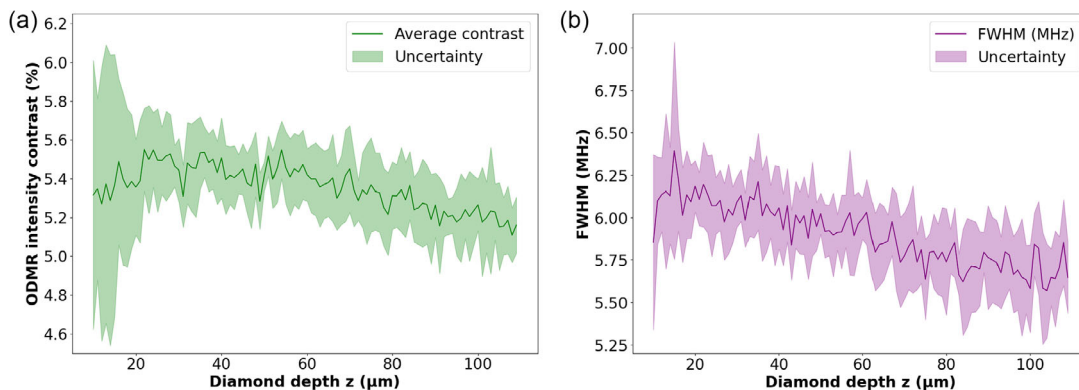


**Figure 9.** Data from different ODMR graphs, obtained at varying planes of the diamond substrate. The data is averaged out of nine different ODMR scans, each starting from a different region of the surface of the diamond. a) Shows the decline in average ODMR intensity contrast. b) Shows the decline in the FWHM of the ODMR peaks.

The contrast of the peaks in an ODMR graph can provide important information on the quality of the color centers. It not only regards the signal-to-noise ratio (SNR), but is also affected by effects of decoherence and inhomogeneous broadening, which significantly impact the optical properties of the emitters. These phenomena can be caused by many factors, including the presence of strain fields, which are investigated here. **Figure 9** demonstrates how contrast deteriorates close to the diamond– $\text{SiO}_2/\text{Si}$  interface. The initial ODMR intensity contrast at the top surface is  $\approx 5.32\%$ , increasing to an average of  $5.51\%$  in the region where the NV centers exhibit the best signal, and finally decreasing to  $\approx 5.15\%$  close to the interface.

The average full width half maximum (FWHM) of the peaks in the ODMR spectra follows a similar trend, as it seems to diminish close to the interface. It drops from an average of  $6.08$  MHz close to the top surface, down to an average of  $5.70$  MHz close to the interface. This is an unexpected result, as one would anticipate that the observed linewidth worsens under increased strain conditions, similar to how contrast decreases.

Regarding the experimental setup, problems occasionally arise when focusing on the back surface of a thick substrate, due to limits

set by the working distance of the objective lens, as well as obstruction by the microwave delivery wire. This necessitates thinning of the diamond layer by  $\text{O}_2$  plasma etching, a rather time-consuming process. Lastly, the ODMR measurement process itself is another factor to take into consideration concerning the quality of the measurements. Long scanning durations make the samples more prone to thermal drifts and can introduce experimental parameter fluctuations. The time inefficiency is further exacerbated by the long direct bonding processing time of approximately a week. It is worth noting that future DOI substrates may be comprised of diamonds with a thickness of a few micrometers or even in the nanometer range. In such cases, the aforementioned strain effects and the quality of the emitters are bound to differ and be more localized.

## 6. Conclusion

Strain characterization was performed on a diamond directly bonded to an insulator substrate ( $\text{SiO}_2/\text{Si}$ ). The mismatch in thermal expansion coefficients between diamond and  $\text{SiO}_2/\text{Si}$  during the direct bonding process induces strain effects, particularly pronounced near the interface. In this study, strain

properties were evaluated across regions exhibiting different bonding conditions by conducting depth-resolved measurements using ODMR. The ODMR technique allowed for the correlation of resonance frequency shifts and splittings to volumetric and shear strain amplitudes, respectively. Results revealed increased lattice deformations when approaching the diamond-SiO<sub>2</sub>/Si interface, with the volumetric strain parameter exhibiting an increase of 0.45 MHz and the shear strain parameter rising by 0.71 MHz. Additionally, PL mapping of partially bonded diamond areas identified interference fringes that likely indicate localized strain or imperfect bonding at the interface. In this investigation, only minor changes in ODMR contrast and linewidth were observed, suggesting negligible deterioration in emitter quality. Specifically, contrast deteriorated by ≈0.36%, while unexpectedly, the linewidth FWHM also decreased by 0.38 MHz. In conclusion, we have determined that PL mapping serves as an effective preliminary method for assessing bonding quality, while ODMR provides detailed insights into the magnitude and nature of strain and its impact on NV centers. Nevertheless, further detailed measurements are required to fully understand how strain influences the optical and electronic properties of color centers in directly bonded diamond substrates.

## Acknowledgements

The authors were gratefully acknowledge support from the joint research program “Modular quantum computers” by Fujitsu Limited and Delft University of Technology, co-funded by the Netherlands Enterprise Agency under project number PPS2007.

## Conflict of Interest

The authors declare no conflict of interest.

## Data Availability Statement

The data that support the findings of this study are available from the corresponding author upon reasonable request.

## Keywords

diamond-on-insulator, direct bonding, nitrogen-vacancy centers, optically detected magnetic resonance, photoluminescence mapping, strain effects, thermal expansion mismatch

Received: March 31, 2025

Revised: June 21, 2025

Published online:

- [1] A. Faraon, C. Santori, Z. Huang, V. M. Acosta, R. G. Beausoleil, *Phys. Rev. Lett.* **2012**, 109, 033604.
- [2] J.-C. Arnault, S. Saada, V. Ralchenko, *Phys. Status Solidi RRL* **2022**, 16, 2100354.
- [3] S. W. Ding, M. Haas, X. Guo, K. Kuruma, C. Jin, Z. Li, D. D. Awschalom, N. Deegan, F. J. Heremans, A. High, M. Lončar (Preprint) arXiv:2402.05811, Submitted: 2024, <https://arxiv.org/abs/2402.05811>.

- [4] R. Ishihara, J. Hermias, S. Yu, K. Y. Yu, Y. Li, S. Nur, T. Iwai, T. Miyatake, K. Kawaguchi, Y. Doi, S. Sato, in *Proc. IEEE Int. Electron Devices Meet. (IEDM)*, Piscataway, New Jersey, USA **2021**, pp. 14.5.1–14.5.4, <https://doi.org/10.1109/IEDM19574.2021.9720552>.
- [5] P. E. Barclay, K.-M. C. Fu, C. Santori, A. Faraon, R. G. Beausoleil, *Phys. Rev. X* **2011**, 1, 011007.
- [6] M. Ruf, N. H. Wan, H. Choi, D. Englund, R. Hanson, *J. Appl. Phys.* **2021**, 130, 070901.
- [7] K. Ngan, Y. Zhan, C. Dory, J. Vučković, S. Sun, *Nano Lett.* **2023**, 23, 9360.
- [8] S. Mi, M. Kiss, T. Graziosi, N. Quack, *J. Phys.: Photonics* **2020**, 2, 042001.
- [9] F. Lenzini, N. Gruhler, N. Walter, W. H. P. Pernice, *Adv. Quantum Technol.* **2018**, 1, 1800061.
- [10] S. Sun, J. L. Zhang, K. A. Fischer, M. J. Burek, C. Dory, K. G. Lagoudakis, Y.-K. Tzeng, M. Radulaski, Y. Kelaita, A. Safavi-Naeini, Z.-X. Shen, N. A. Melosh, S. Chu, M. Lončar, J. Vučković, *Phys. Rev. Lett.* **2018**, 121, 083601.
- [11] T. Chen, J. Hermias, S. Nur, R. Ishihara, *Appl. Phys. Lett.* **2025**, 126, 231901.
- [12] V. Masteika, J. Kowal, N. St, *ECS J. Solid State Sci. Technol.* **2014**, 3, Q42.
- [13] T. Matsumae, Y. Kurashima, H. Umezawa, H. Takagi, *Jpn. J. Appl. Phys.* **2019**, 59, SBBA01.
- [14] T. Plakhotnik, M. W. Doherty, J. H. Cole, R. Chapman, N. B. Manson, *Nano Lett.* **2014**, 14, 4989.
- [15] A. Berzins, J. Smits, A. Petruhins, R. Rimsa, G. Mozolevskis, M. Zubkins, I. Fescenko, *Opt. Express* **2023**, 31, 17950.
- [16] E. Oliveira, C. Li, X. Zhang, A. Puthirath, M. R. Neupane, J. Weil, A. G. Birdwell, T. Ivanov, S. Kong, T. Grey, H. Kannan, *MRS Adv.* **2022**, 7, 543.
- [17] T. Matsumae, Y. Kurashima, H. Takagi, H. Umezawa, E. Higurashi, *Scr. Mater.* **2021**, 191, 52.
- [18] C. Malhaire, M. Granata, D. Hofman, A. Amato, V. Martinez, G. Cagnoli, A. Lemaître, N. Shcheblanov, *J. Vac. Sci. Technol. A* **2023**, 41, 043401.
- [19] I. Vlasov, V. Ralchenko, D. Zakharov, N. Zakharov, *Phys. Status Solidi A* **1999**, 174, 11.
- [20] S. Stoupin, Y. V. Shvyd'ko, *Phys. Rev. B* **2011**, 83, 104102.
- [21] F. Jansen, M. A. Machonkin, N. Palmieri, D. Kuhman, *Appl. Phys. Lett.* **1987**, 50, 1059.
- [22] H. Tada, A. E. Kumpel, R. E. Lathrop, J. B. Slanina, P. Nieva, P. Zavracky, I. N. Miaoulis, P. Y. Wong, *J. Appl. Phys.* **2000**, 87, 4189.
- [23] K. G. Lyon, G. L. Salinger, C. A. Swenson, G. K. White, *J. Appl. Phys.* **1977**, 48, 865.
- [24] C. A. Swenson, *J. Phys. Chem. Ref. Data* **1983**, 12, 179.
- [25] J. T. L. Gamler, A. Leonardi, X. Sang, K. M. Koczur, R. R. Unocic, M. Engel, S. E. Skrabalak, *Nanoscale Adv.* **2020**, 2, 1105.
- [26] R. H. Doremus, *J. Electrochem. Soc.* **1987**, 134, 2001.
- [27] D. A. Broadway, B. C. Johnson, M. S. J. Barson, S. E. Lillie, N. Donschuk, D. J. McCloskey, A. Tsai, T. Teraji, D. A. Simpson, A. Stacey, J. C. McCallum, J. E. Bradby, M. W. Doherty, L. C. L. Hollenberg, J.-P. Tetienne, *Nano Lett.* **2019**, 19, 4543.
- [28] J. H. N. Loubser, J. A. van Wyk, *Rep. Prog. Phys.* **1978**, 41, 1201.
- [29] P. Udvarhelyi, V. O. Shkolnikov, A. Gali, G. Burkard, A. Pályi, *Phys. Rev. B* **2018**, 98, 075201.
- [30] M. S. Alam, F. Gorini, M. Gawętczyk, D. Wigger, G. Coccia, Y. Guo, S. Shahbazi, V. Bharadwaj, A. Kubanek, R. Ramponi, P. E. Barclay, A. J. Bennett, J. P. Hadden, A. Bifone, S. M. Eaton, P. Machnikowski, *Phys. Rev. Appl.* **2024**, 22, 024055.